



ELSEVIER

Contents lists available at [SciVerse ScienceDirect](http://www.sciencedirect.com)

Comptes Rendus Mecanique

www.sciencedirect.com

10th International Meeting on Thermodiffusion

On the accuracy of the interdiffusion coefficient measurements of high-temperature binary mixtures under ISS conditions

Núria Saez^a, Xavier Ruiz^{a,b,*}, Jordi Pallarés^c, Valentina Shevtsova^d^a Dept. Química Física i Inorgànica, Universitat Rovira i Virgili, Tarragona, Spain^b Institut d'Estudis Espacials de Catalunya, IEEC, Barcelona, Spain^c Mechanical Engineering Department, Universitat Rovira i Virgili, Tarragona, Spain^d MRC, ULB, EP, CP165/62, Dept. Chemical Physics, B1050, Brussels, Belgium

ARTICLE INFO

Article history:

Available online 15 March 2013

Keywords:

High-temperature binary mixtures

Photovoltaic Si

Al–Cu binary alloys

Low-gravity environments

Interdiffusion coefficient accuracy

ABSTRACT

An accelerometric record from the IVIDIL experiment (ESA Columbus module) has exhaustively been studied. The analysis involved the determination of basic statistical properties as, for instance, the auto-correlation and the power spectrum (second-order statistical analyses). Also, and taking into account the shape of the associated histograms, we address another important question, the non-Gaussian nature of the time series using the bispectrum and the bicoherence of the signals. Extrapolating the above-mentioned results, a computational model of a high-temperature shear cell has been performed. A scalar indicator has been used to quantify the accuracy of the diffusion coefficient measurements in the case of binary mixtures involving photovoltaic silicon or liquid Al–Cu binary alloys. Three different initial arrangements have been considered, the so-called interdiffusion, centred thick layer and the lateral thick layer. Results allow us to conclude that, under the conditions of the present work, the diffusion coefficient is insensitive to the environmental conditions, that is to say, accelerometric disturbances and initial shear cell arrangement.

© 2013 Académie des sciences. Published by Elsevier Masson SAS. All rights reserved.

1. Introduction

The accurate determination of interdiffusion coefficients is of capital importance for the knowledge and control of solidification processes [1–3]. In effect, interdiffusion coefficients are usually treated as constants in computational growth models, but real systems with large segregation coefficients need the consideration of concentration and position-dependent diffusion coefficients because of the strong gradients generated at the growing interfaces. The knowledge of these dependences could help to improve the accuracy of the numerical predictions. In addition, concentration gradients are correlated with chemical potential gradients, so it is very important to deep also in the determination and understanding of such relationships in order to be properly applied in the predictive growth models. In the present work we particularize these aspects for two different kinds of materials certainly relevant in our daily technology, photovoltaic silicon and aluminium-based alloys.

Concerning multi-crystalline ingots of photovoltaic silicon, PV-Si, it is interesting to remember that, for economical reasons, that is to say, to attain parity (cost of solar energy equal to costs of conventional energy sources), upgraded metallurgical grade silicon, UMG-Si, is progressively replacing the more expensive ultra pure electronic grade silicon, EG-Si, as feedstock material in ingot casting processes. But UMG-Si contains a high amount of dopants, metallic and non-metallic impurities that strongly interact with crystal defects in the resulting multi-crystalline ingots. Precise data about diffusion

* Corresponding author at: Dept. Química Física i Inorgànica, Universitat Rovira i Virgili, Tarragona, Spain.

E-mail address: josepxavier.ruiz@urv.cat (X. Ruiz).

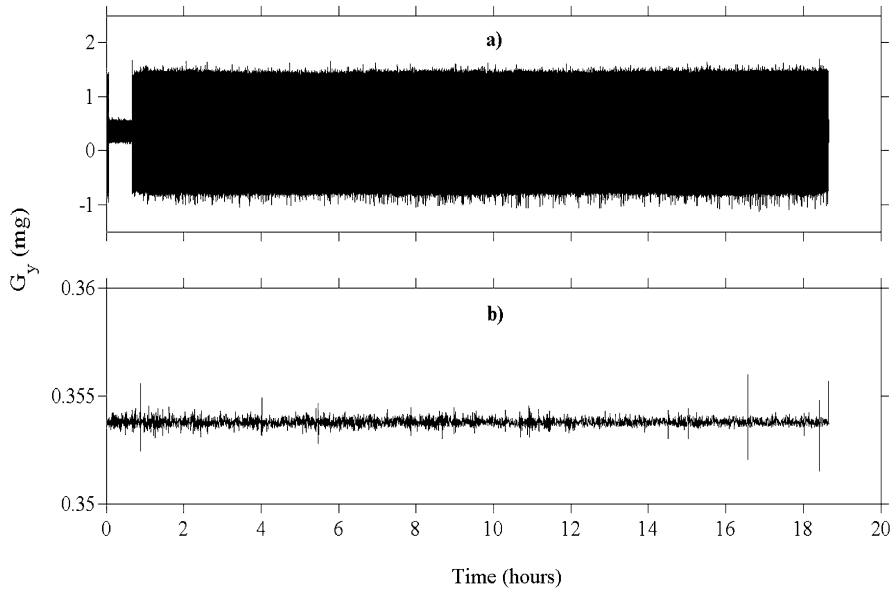


Fig. 1. (a) Time evolution of G_y . (b) 10-s interval average G_y signal.

coefficients of dopants and impurities are also of capital importance for the accuracy of the predictions obtained with computational growth models [4,5]. Concerning metallic alloys, in particular, Al-based alloys, interdiffusion and their relation to thermodynamics play a capital role in nucleation theories and in the correct predictions of the coupled macro-meso-microscopic computational models of solidification [6–8].

Interdiffusion coefficients are measured using shear cells and long-capillaries. In the shear cell case, the quantitative determination of the interdiffusion coefficients is made by the use of chemical analyses of the solidified samples and by applying Fick's diffusion laws. Recently, X-ray radioscopic techniques allow instantaneous measurements of concentration profiles by taking absorption pictures of capillary experiments [9]. Space environments seem to be an excellent choice for estimating diffusion coefficient measurements, but a difficult factor to control there is the effect of residual accelerations, which are potential sources of convective disturbances. To assess the real importance of such effects, a real accelerometric scenario will be characterized in detail here and, extrapolating this characterization, numerical calculations using a model of shear cell will enable us to evaluate the accuracy in the measure of the mass transport coefficient.

2. Model considerations

2.1. Accelerometric analyses

The accelerometric record analyzed here covers a period of 18 h, 36 min and 11.5 s of the IVIDIL experiment (run number 29), with a sampling rate of 500 Hz and a cut-off frequency of 200 Hz [10–13]. Due to the fact that the internal shaking direction of the above-mentioned experiment is in the direction of the y axis, in the present study we report the results concerning only the G_y signal. Fig. 1a shows the time series of G_y . It is clear that this raw information is not easy to understand and manipulate in direct format. To do so, different alternatives are used in the literature. One of them involves the so-called interval average acceleration versus time. That is to say, analytically,

$$\tilde{G}_y(k) = \frac{1}{M} \sum_{i=1}^M G_y((k-1)M + i), \quad k = 1, \dots, \frac{N}{M} \quad (1)$$

where M is the length of the interval and N the length of the whole signal. Local averages enable us to smooth the appearance of the huge amount of data, allowing longer periods of time to be more clearly plotted. But the information to be extracted is more restrictive because interval averaged results are only useful to identify overall effects that tend to cause changes of the mean acceleration level. In the present case (see Fig. 1b), and independently of the time interval used for averaging, the mean g -level remains practically constant all along the duration of the run.

The power spectral density, equivalently the energy distribution for the different frequencies of the spectrum, has been estimated here using the periodogram. This means:

$$PSD_k = \frac{|FFT_k|^2}{N \cdot f_N \cdot U} \quad (2)$$

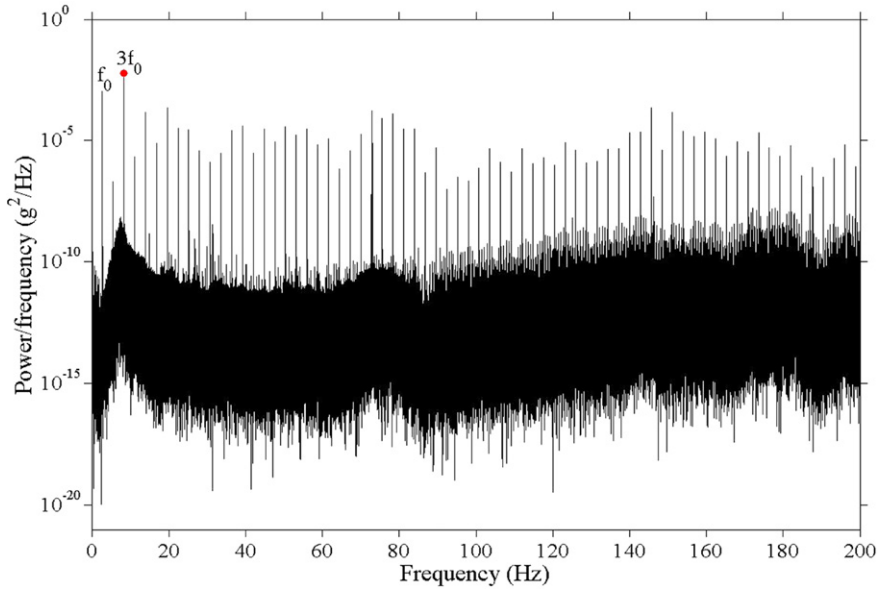


Fig. 2. Power spectral density of G_y .

where FFT_k is the fast Fourier transform of the signal, N its length, f_N the associated Nyquist frequency and U a characteristic value function of the window w_n applied obtained as $U = \frac{1}{N} \sum_{n=0}^{N-1} w_n^2$. In this work, the power spectral density has been evaluated using four window types, rectangular, Blackman, Hanning, and Bartlett. Results concerning the frequency distribution are invariant and, as can be seen in Fig. 2, the peak of the fundamental frequency, $f_0 = 2.8$ Hz, coinciding with the frequency of the shaking motor, is not as energetic as the $3f_0$ harmonic. The rest are practically negligible. This fact reasonably supports the idea that the signal could be approached as a constant value – the average – plus only another one single frequency centred at the most energetic $3f_0$ harmonic. The amplitudes can be readily estimated from the FFT transform. Similar procedures with the other two components of acceleration, G_x and G_z , give finally the following results – in g units – for the components of the gravity vector $\vec{G}(t) = \vec{G}_0 + \vec{G}_v \cdot \sin(2\pi \vec{F}t)$ considered here as,

$$G_x(t) = G_{0,x} + G_{v,x} \cdot \sin(2\pi F_x t) = 0.0003 + 0.0005 \cdot \sin(219.2\pi t) \tag{3}$$

$$G_y(t) = G_{0,y} + G_{v,y} \cdot \sin(2\pi F_y t) = 0.0008 + 0.0001 \cdot \sin(16.8\pi t) \tag{4}$$

$$G_z(t) = G_{0,z} + G_{v,z} \cdot \sin(2\pi F_z t) = -0.0004 + 0.0004 \cdot \sin(162.4\pi t) \tag{5}$$

The moment of second order of the discrete accelerometric signal, that is to say, the auto-correlation function, is a measure of how much a signal at time t is like itself at some other time $t + \tau$. Analytically,

$$R_{YY}(L) = \frac{\sum_{j=1}^{N-L} \{G_y(j-1) - \bar{G}_y\} \{G_y(j-1+L) - \bar{G}_y\}}{\sum_{j=1}^N \{G_y(j-1) - \bar{G}_y\}^2} \tag{6}$$

where G_y is the signal under study and \bar{G}_y its mean. Positive auto-correlation might be considered a tendency for a system to remain in the same state from one observation to the next. So, physical and mechanical systems usually give values typically positive because of the inertia of its constituents. However, in the present case, the correlogram of the signal G_y , plotted in Fig. 3, exhibits a typical pattern, characteristic of data coming from an underlying harmonic system. The decrease is simply due to the finite length of the window used.

Fig. 4 shows the histogram of the time series associated with the same y acceleration component. The histogram, comprising 100 bins, clearly shows a multimodal behaviour. The inset of Fig. 4 presents a box plot with additional accelerometric details. Remember that this kind of plot gives a clear idea about the smallest and largest data, the median, the lower/first quartile (Q1) and the upper/third quartile (Q3). The length of the upper and lower whiskers in the figure has been calculated, as usual, as $Q3 + 1.5(Q3 - Q1)$ and $Q1 - 1.5(Q3 - Q1)$, respectively.

In addition to the quantitative description offered by the box plot, an interesting consequence of the shape of the histogram is that the accelerometric signals are non-Gaussian. To collect additional information about the deviations from Gaussianity of the signals, we concentrate here on the study of the Fourier spectrum of the third-order cumulant, that is to say, on the bispectrum [14–17]. Fig. 5a shows a section of the third-order cumulant enhancing the fact that the zero-lagged value, the skewness, is not zero. Remember that, similar to the way in which the variance of the process is related with its power spectrum and with its auto-correlation (second-order cumulant), the skewness of the process is

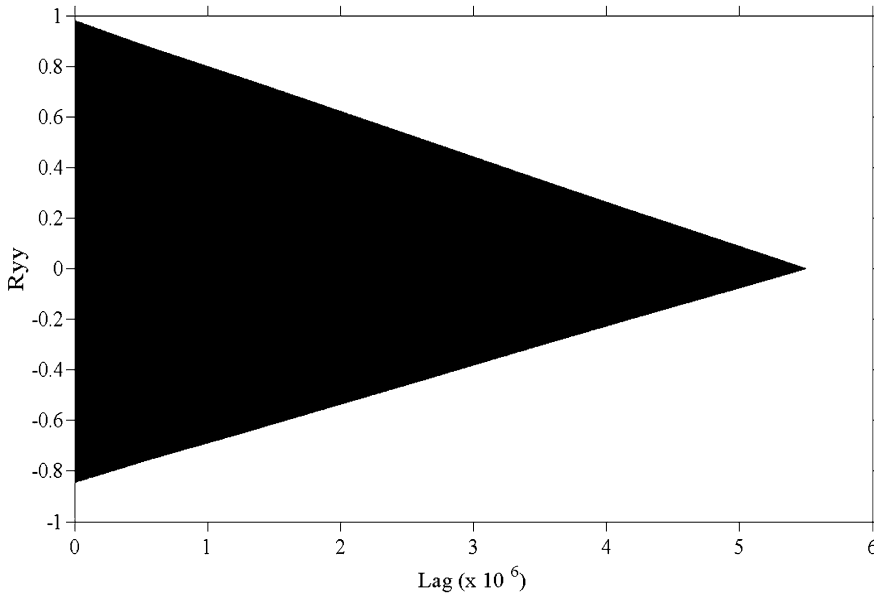


Fig. 3. Correlogram of the y component of acceleration.

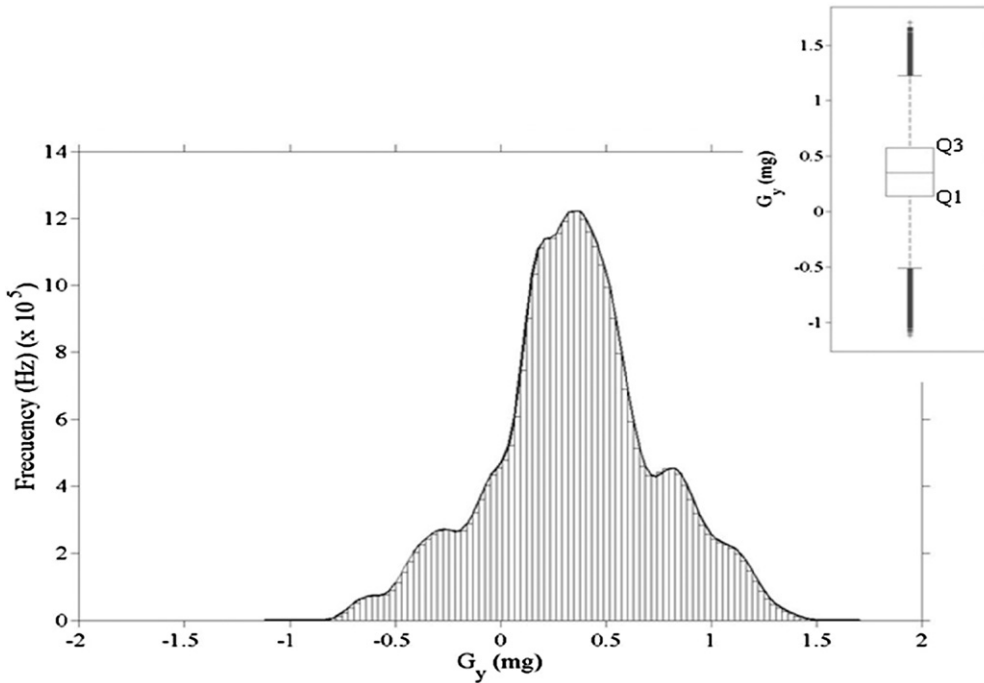


Fig. 4. Histogram associated with the G_y signal (the inset shows the box plot of the same accelerometric component).

related with its bispectrum and with the zero-lag cumulant of third order. Fig. 5b shows the surface plot of the bispectrum associated with G_y . The main peak is located at $(f_0, 2f_0)$, whereas another less intense ones are also detected at (f_0, f_0) and $(3f_0, 3f_0)$. The rest are meaningless because of the symmetries of the standard representation used. Notice that, despite the literature claims the ability of the Hamming window to resolve quadratic frequency coupling peaks [18], we did not detect any significant difference between the results obtained using another kind of window as, for instance, Blackman, Hanning or Bartlett type.

A squared normalized version of the bispectrum, that is to say the bicoherence, is also calculated for completeness. With both tools we investigate the existence of quadratic frequency coupling. Remember that frequency coupling between two frequency components of a signal results in a contribution at a frequency equal to their sum. These additional harmonics,

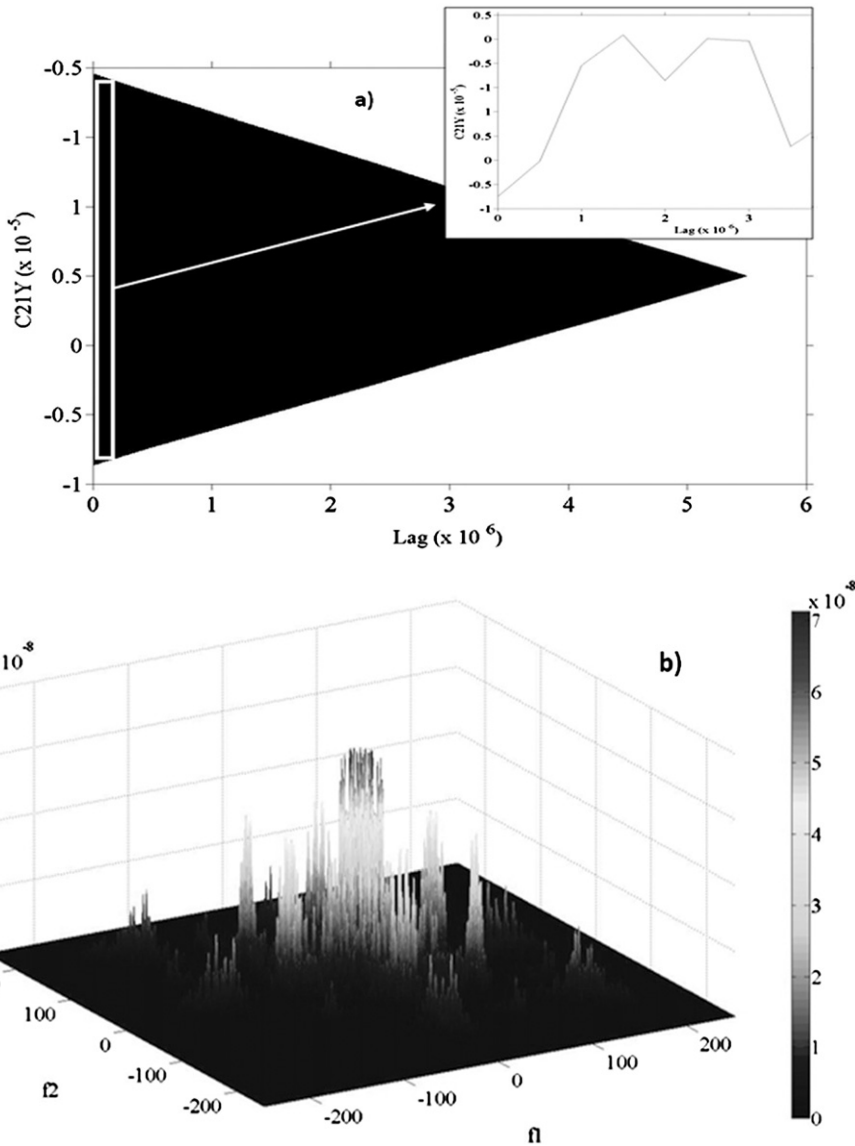


Fig. 5. (a) A section of the third-order cumulant. (b) Bispectrum of the G_y signal.

called distortion harmonics, could also be phase coupled to the original ones and, in this case, the nonlinearity is called quadratic phase coupling. Fig. 6 shows the bicoherence of the G_y signal with a maximum located at the same place ($f_0, 2f_0$) as the main peak in the bispectrum and with an amplitude of roughly 0.8. This fact shows that f_0 and $2f_0$ are frequency coupled and indicates that roughly the 80% of the amplitude associated with the $3f_0$ harmonic is generated by quadratic frequency coupling.

The presence of this coupling is probably related with some anomalous nonlinear modes of operation of the internal machinery (dry friction, ball bearings malfunction...) which transfers energy in a special way between the different harmonics [19,20].

2.2. Numerical procedures

In order to analyze convective disturbances generated by the peculiar accelerometric environment associated with the International Space Station, ISS, we use the following transport equations for the velocity, \vec{V} , temperature T and concentration C in non-dimensional form:

$$\vec{\nabla} \cdot \vec{V} = 0 \tag{7}$$

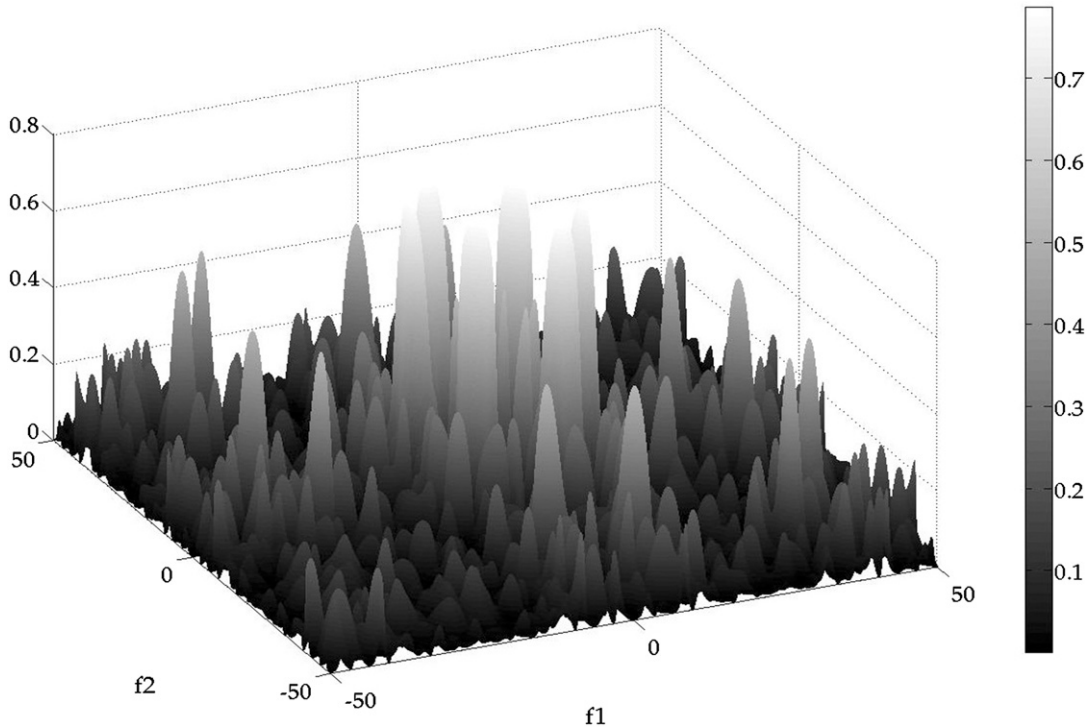


Fig. 6. Bicoherence of the G_y signal.

$$\frac{D\vec{V}}{Dt} = -\vec{\nabla}p + Sc\nabla^2\vec{V} - \vec{B}(t) \tag{8}$$

$$\frac{DT}{Dt} = \frac{Sc}{Pr}\nabla^2T \tag{9}$$

$$\frac{DC}{Dt} = \nabla^2C \tag{10}$$

with $\vec{B}(t)$ the buoyancy term, that for a general thermosolutal case can be written as,

$$\vec{B}(t) = \vec{B}_c(t) + \vec{B}_T(t) \tag{11}$$

with,

$$\vec{B}_c(t) = \{ \vec{R}a_0^c + \vec{R}a_v^c \cdot \sin(2\pi \vec{F}t) \} \cdot Sc \cdot C \tag{12}$$

$$\vec{B}_T(t) = \{ \vec{R}a_0^T + \vec{R}a_v^T \cdot \sin(2\pi \vec{F}t) \} \cdot \frac{Sc^2}{Pr} \cdot T \tag{13}$$

being the constant solutal and thermal Rayleigh numbers $\vec{R}a_0^c = \frac{\vec{G}_0\beta_c\Delta C^*H^3}{\nu D}$, $\vec{R}a_0^T = \frac{\vec{G}_0\beta_T\Delta T^*H^3}{\nu\alpha}$ and the solutal and thermal vibrational Rayleigh numbers are $\vec{R}a_v^c = \frac{\vec{G}_v\beta_c\Delta C^*H^3}{\nu D}$, $\vec{R}a_v^T = \frac{\vec{G}_v\beta_T\Delta T^*H^3}{\nu\alpha}$. The Schmidt and Prandtl numbers are $Sc = \frac{\nu}{D}$ and $Pr = \frac{\nu}{\alpha}$ respectively. In addition, ν is the kinematic viscosity, β_c the solutal expansion coefficient, D the nominal diffusion coefficient needed for calculations, β_T the thermal expansion coefficient and α the thermal diffusivity.

The length and time scales used to obtain the previous non-dimensional variables are the diameter of the cylindrical shear cell H and the dimensional group H^2/D , respectively. The non-dimensional concentrations and temperatures are defined as $C = (C^* - C_0^*)/\Delta C^*$ and $T = (T^* - T_0^*)/\Delta T^*$, where ΔC^* is the dimensional initial concentration difference and ΔT^* is the temperature difference between both the hot and cold sides of the cell.

Concerning the different thermo-physical parameters needed in the calculations, Table 1 shows a typical set of values extracted from the literature for the two materials considered, photovoltaic silicon [4] and aluminium-based alloys [6,7]. Notice that in the case of the photovoltaic silicon and due to the considerable difference in the diffusion coefficients corresponding to dopants and metallic impurities, we finally considered two different sets of parameters. No temperature and concentration dependences of the above-mentioned parameters have been considered here. Also, supposing that the micro-gravity globe box is accelerometrically equivalent to the materials science research rack [21], the extrapolated gravity vector components appearing now in the definition of the different Rayleigh numbers are the ones labelled as (3), (4), (5).

Table 1
Thermophysical dataset used in the present calculations.

	Photovoltaic Si (dopants/metallic impurities)	Al-based alloys
L (cm)	6	6
H (cm)	0.15	0.15
$10^3 \nu$ (cm ² s ⁻¹)	3.4	5.25
$10^5 D$ (cm ² s ⁻¹)	12/100	3.5
$10^2 \beta_c \Delta c^*$	2.5	-4
Sc	28.3/3.4	150
$\bar{R}a_0^c$	dopants: (62.1, 165.6, -82.8) metallic imp.: (7.4, 19.8, -9.9)	(-220.4, -587.8, 293.9)
$\bar{R}a_v^c$	dopants: (103.5, 20.7, 82.8) metallic imp.: (12.4, 2.5, 9.9)	(-367.4, -73.5, -293.9)
$10^2 \alpha$ (cm ² s ⁻¹)	15	10
$10^4 \beta_T$ (K ⁻¹)	3	3
$\Delta T_{\text{longitudinal}}^*$ (K)	5	5
Pr	0.023	0.05
($\times 10^3$) $\bar{R}a_0^T$	(3.0, 8.0, -4.0)	(2.9, 7.7, -3.8)
($\times 10^3$) $\bar{R}a_v^T$	(5.0, 1.0, 4.0)	(4.8, 1.0, 3.8)

Shear cell boundaries have been considered as no-slip and impermeable. Thermal gradients have been modelled by imposing a constant temperature difference between both hot and cold sides. The lateral side of the cylinder has simply been defined as adiabatic. Temperature differences are small enough to neglect here thermodiffusion – Soret – effects. From the point of view of concentration and to be as general as possible, the present work considers three different initial configurations [22,23]. In the first one, called interdiffusion-couple the diffusion is driven by the existence of two half parts with different initially uniform concentrations located symmetrically at both sides of the cylindrical cell. In the second one, the centred thick layer configuration, the initially uniform source of concentration is located in the central part of the cell in such a way that diffusion proceeds symmetrically at both sides of it. If that source is situated in one side only, not in the centre, the diffusion takes place all along the cell and the arrangement is now designed here as a lateral thick layer configuration – also long-capillary in the literature.

Because the shear cells are segmented cylinders, the number of segments of the cell has been set at twenty. But, in the centred arrangement, the number has been increased to twenty-one to preserve the symmetry of propagation of the solute. In terms of absolute measures, the diameter of each cell segment is 0.15 cm and its length is 0.30 cm. In this way, the total length of the standard cell used here is 6 cm and the inner diameter 0.15 cm.

Thermosolutal calculations initially start considering uniform fields in the domain at rest so no concentration scatter is possible within a given sample by, for instance, insufficient quenching rate in the experimental elaboration. The diffusion coefficient needed for the calculations – the reference value – D , has been considered constant, that is to say independent of the composition. To accomplish this hypothesis, the quantitative difference between the concentrations should be limited to a reasonable threshold value, say, at much, of the order of 5 wt%.

The non-dimensional transport equations together with the corresponding set of boundary and initial conditions have numerically been solved using a domestic finite-volume code [22]. In the 2D case, the value of the different non-dimensional numbers associated with the present problem is given in Table 1. Structured rectangular meshes of 42 360 (1060 × 41), 37 040 (927 × 41) and 36 200 (906 × 41) rectangular elements have been used in the interdiffusion-couple, centred and lateral thick layer configurations, respectively. In the 3D case, an unstructured mesh arrangement of 610 000 cells has been used only to make calculations in the interdiffusion-couple configuration. For the sake of brevity, mesh details can be consulted in the literature [22–25].

If the convection is intense enough, the reference diffusion coefficient D will change to a different one $D^*(t)$. The calculation of this new diffusion coefficient $D^*(t)$ in the interdiffusion-couple configuration involves the slope determination of the linear fit for the following set of values $\{(x_i, 2 \cdot \sqrt{t} \cdot \text{erf}^{-1}(-2 \cdot c_i(t, x)))\}$, $\forall i = 1, 20$. In this expression, x_i is the position of the centre of each segment of the cell, t the corresponding time, erf^{-1} the inverse of the Gauss error function and $c_i(t, x) = \frac{1}{S} \cdot \iint c(t, x, y) dx dy$, the segment-averaged computed concentration. Calculations of $D^*(t)$ in the cases of the centred and lateral thick layer configurations involved the direct minimization of the χ^2 -type residual, $\Xi(t, D^*)$,

$$\Xi(t, D^*) = \sum_{i=1}^N (c_i(t, x_i) - c(t, x_i; D^*))^2 \tag{14}$$

because of the analytical solution of the diffusion of a planar thick source into a couple of semi-infinite liquid domains is:

$$c(t, x; D) = \frac{1}{2} \left[\left\{ \text{erf} \left(\frac{h+x}{2\sqrt{D \cdot t}} \right) + \text{erf} \left(\frac{h-x}{2\sqrt{D \cdot t}} \right) \right\} - 1 \right] \tag{15}$$

and also the analytical solution accounting for diffusion into a single semi-infinite domain is:

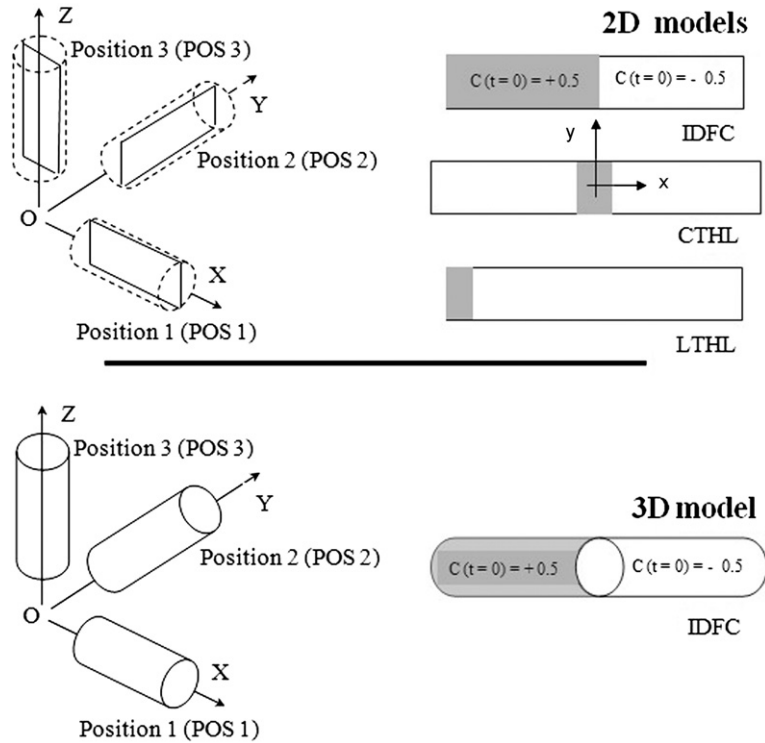


Fig. 7. Sketch of the three orientations used in the present numerical study.

$$c(t, x; D) = \frac{1}{2} \left[\left\{ \operatorname{erf} \left(\frac{2h + (x + \frac{1}{2})}{2\sqrt{D \cdot t}} \right) + \operatorname{erf} \left(\frac{2h - (x + \frac{1}{2})}{2\sqrt{D \cdot t}} \right) \right\} - 1 \right] \quad (16)$$

with L the total length of the cell and h half of the length of the initial central source segments or the length of the initial lateral source segments. The final evaluation of the time-dependent error – in percentage – uses the standard non-dimensional indicator:

$$\%D^*(t) = 100 \cdot \frac{D^*(t) - D}{D} = 100 \cdot \left\{ \frac{D^*(t)}{D} - 1 \right\} \quad (17)$$

Calculations of $D^*(t)$ use only active segments, that is to say, segments in which the variation of the averaged concentration is greater than the 1% of the initial one. This choice is equivalent to admit a 1% error in the chemical determination of the averaged concentration in each solid fragment by usual solid-state techniques of analysis as, for example, atomic absorption spectroscopy, secondary ion mass spectroscopy or electron probe micro analysis.

Finally, in order to satisfy the mathematical hypothesis of infinitely long domains, calculations finished when the first or the last – or both simultaneously – segments become active segments. The time needed to attain these final conditions is called the end time, t_{end} , and gives us a final unique value $\%D^*(t = t_{\text{end}})$. This computational strategy avoids the necessity to consider the end time as a parameter to be simultaneously determined during the experiments, as really occurs in the experiments.

3. Results and discussion

3.1. 2D calculations

As a first approximation to the problem and to alleviate as much as possible the computational effort associated with the diffusive processes, the shear cell has been firstly considered as rectangular, in particular, a plane array of rectangular interconnected elements – called ‘plane segments’. Fig. 7 shows the three orientations considered in this study. From the point of view of the previous gravity vector, position 1, POS 1, uses the x and z components, while position 3, POS 3, uses a different couple, the z and x components. Finally, the so-called position 2, POS 2, uses G_y and G_z . In addition, each orientation covers the three possible above-mentioned arrangements, interdiffusion, IDFC, centred thick layer, CTHL and lateral thick layer, LTHL, respectively. Notice that in order to follow properly the fast oscillations of the gravity components, the increment of time, Δt , has been chosen to ensure more than twenty computational steps per oscillation in all cases.

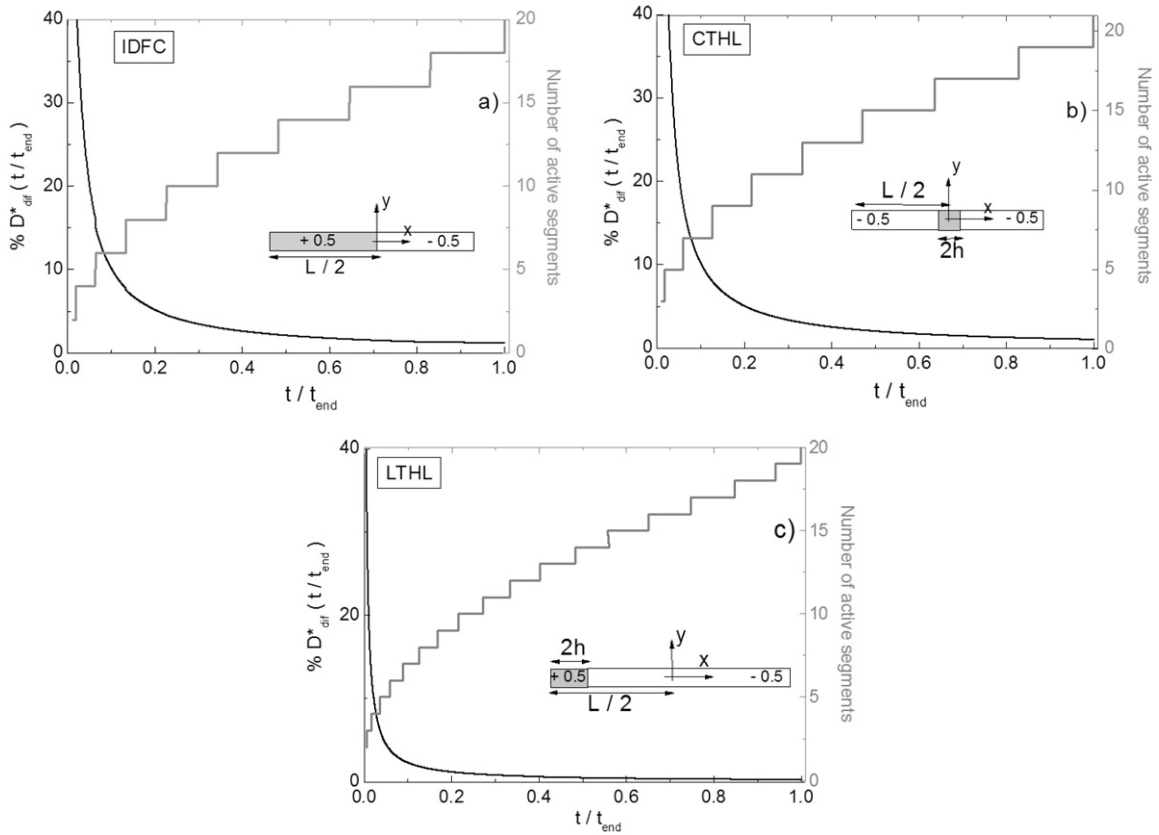


Fig. 8. Summary of computational results obtained in the pure diffusive case (2D calculations) for: (a) interdiffusion, (b) centred thick layer, (c) lateral thick layer arrangements.

This implied that calculations required an extremely hard computational effort to cover the diffusion process all along the cylindrical cell.

But, in a first place, Fig. 8 shows the temporal evolutions of $%D_{dif}^*(t)$ associated with the three diffusive configurations. The non-zero values of this magnitude at $t = t_{end}$ have been considered as systematic errors associated with the present methodology. It is interesting to note that the correlation between the change in the number of active segments and the jumps in the evolution of the $%D_{dif}(t)$ curve is not clear in the centred or lateral thick layer arrangements, even in the first part of the process, in which the concentration gradients are the most important ones. On this matter, it can be observed that the number of segments increases twice only in both the IDFC and CTHL configurations due to the symmetry of propagation of the solute. This symmetry is broken in the lateral thick layer configuration and the evolution of the number of active segments change now one at a time.

Several time histories of $%D^*(t)$ are plotted in Fig. 9. Notice that the curves are not correlated with the external harmonic signals applied due to the nonlinear character of the mathematical manipulations made in the post-processing procedures. So, considering only the information included in $%D^*(t)$, it is not possible to go backwards and characterize the properties of the external signal acting on the liquid system. In addition, Fig. 9 shows that the time evolution of $%D^*(t)$ is similar in all cases, independently of the dopant and of the arrangement used.

Notice that the x axis is normalized in order to compare the three arrangements using the same scale of time, but one must take this normalization cautiously because the end time is different in the three cases. Interdiffusion and centred thick layer arrangements have similar values, but lateral thick layer multiplies by four this value [22,23].

Finally, Table 2 summarizes the results of all 2D calculations made here in terms of $%D(t_{end})$, the final inaccuracy indicator of the diffusion process. This value is equal to the difference between $%D^*(t = t_{end})$ and $%D_{dif}^*(t = t_{end})$ in order to properly correct the systematic errors of the diffusive cases. The lowest values appear in the case of metallic impurities diffusing in photovoltaic silicon, while that the highest ones correspond to generic binary Al–Cu alloys. Also, $%D(t_{end})$ depends on the arrangement used, that is to say, interdiffusion gives the highest values, while the lateral thick layer provides the lowest ones. But, in all cases, the inaccuracy indicator is lower than 1%, ensuring a value lower than the typical resolution error of the experimental analyses. The results obtained using constant values, without the harmonic parts, are also presented in the same table and are practically of the same order. This corroborates the fact that the accuracy is not sensitive to vibrations of the order of several Hertz in any of the arrangements considered [22,23].

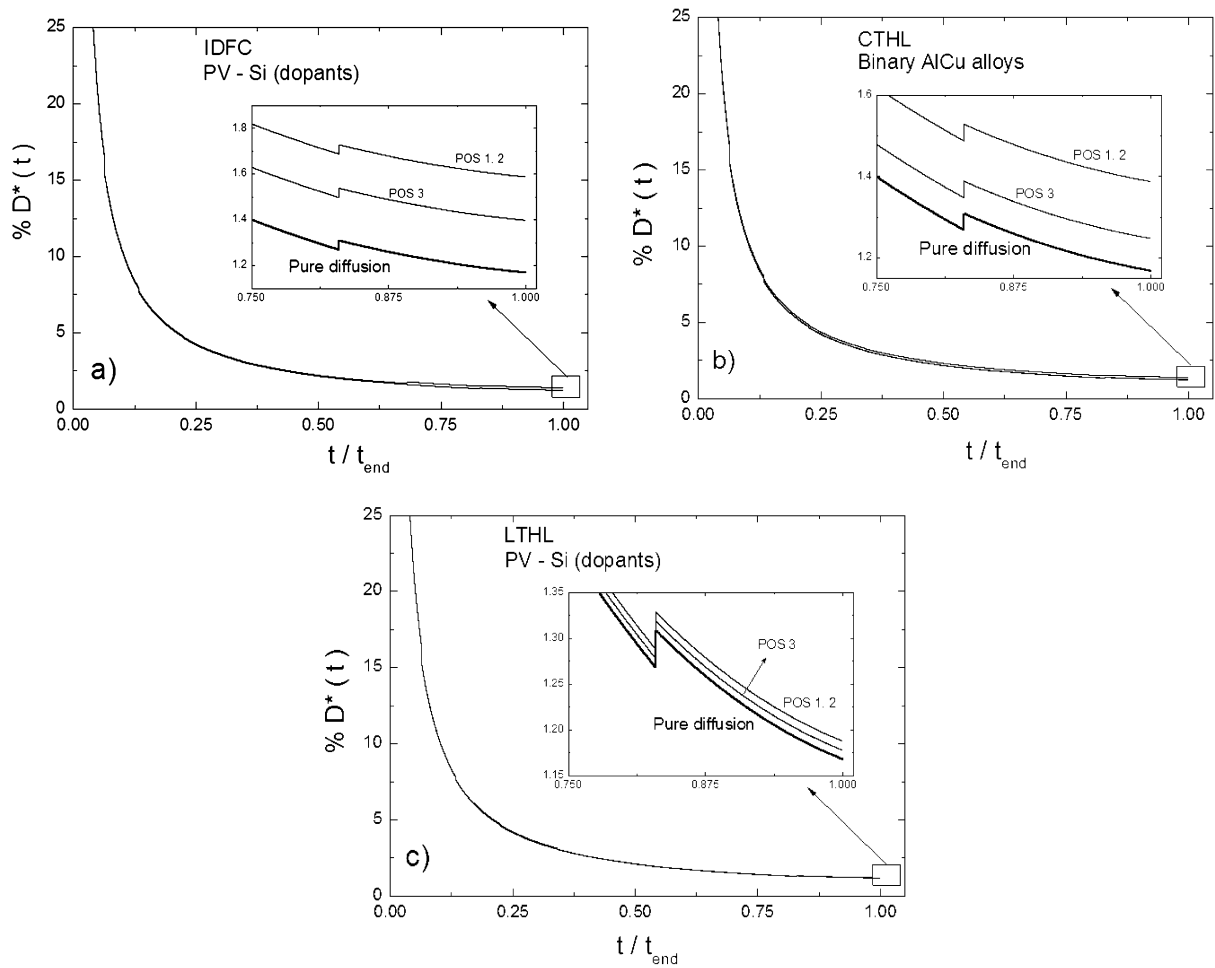


Fig. 9. Time evolution of the inaccuracy indicator $\%D^*(t_{\text{end}})$ for several arrangements and dopants (2D calculations).

Table 2

2D values of the inaccuracy indicator $\%D(t_{\text{end}})$. In the case of photovoltaic silicon, the results correspond to dopants/metallic impurities.

		Gravity	POS 1	POS 2	POS 3
IDFC	Photovoltaic Si	Constant	0.42/0.12	0.42/0.11	0.21/0.07
		Vibratory	0.42/0.12	0.41/0.09	0.22/0.08
CTHL	Binary Al–Cu alloys	Constant	0.84	0.83	0.59
		Vibratory	0.83	0.82	0.60
LTHL	Photovoltaic Si	Constant	0.15/0.06	0.15/0.06	0.08/0.02
		Vibratory	0.16/0.06	0.15/0.04	0.08/0.03
CTHL	Binary Al–Cu alloys	Constant	0.20	0.19	0.08
		Vibratory	0.21	0.19	0.07
LTHL	Photovoltaic Si	Constant	0.07/0.02	0.06/0.01	0.02/0.01
		Vibratory	0.06/0.02	0.07/0.03	0.02/0.01
CTHL	Binary Al–Cu alloys	Constant	0.10	0.09	0.06
		Vibratory	0.09	0.09	0.05

3.2. 3D calculations

In order to minimize the computational effort and based on the results of Table 2, 3D calculations have been selected only for the cases in which the indicator $\%D(t_{\text{end}})$ has a relatively high value. This criterion reduced the forty-eight calculations reported using the 2D approach to only six in 3D – a drastically reduction of roughly the eighty-seven percent. In addition, because 2D results show a clear insensitivity against external vibrations, in our 3D calculations we have considered only a constant gravity, relaxing, in this way, the very restrictive condition on the computational time step. In summary, the

Table 33D values of the inaccuracy indicator $\%D(t_{\text{end}})$ – only constant cases.

		POS 1	POS 2	POS 3
IDFC	Photovoltaic Si	0.19	0.19	0.1
	Binary Al–Cu alloys	0.41	0.4	0.29

six cases consider an interdiffusion arrangement, constant gravity values for the three components of the gravity vector and (i) liquid PV-Si with dopants, (ii) generic binary Al–Cu alloys.

After an identical procedure as in the 2D calculations – including the corresponding corrections due to the purely diffusive case – the final quantitative results are presented in Table 3. Notice firstly that all values are lower than the corresponding ones obtained in the 2D part of the present study. As usual, the presence of a third dimension enables us to numerically relax the quantitative bidimensional results [24,25]. In addition and also in 3D, all six values are also lower than the 1% threshold clearly indicating that, under the present conditions, there is no appreciable impact of the environment in the accuracy of the interdiffusion measurements.

4. Conclusions

Second-order statistical analyses of IVIDIL's run 29 accelerometric record have successfully been performed here, concluding that the most energetic frequency of the signal is not the fundamental one. In addition, the non-Gaussianity of the accelerometric signal associated with the above-mentioned run has been characterized using higher-order statistical analysis techniques. A quadratic frequency coupling has been detected due to malfunctions of the mobile mechanical parts of the shaking motor of the experiment.

Supposing correct enough the extrapolation of this accelerometric behaviour to interdiffusion experimental scenarios, the used simplified translational approach concludes that for real shear cells, independently of the initial arrangement, there is no appreciable convective impact on the accuracy of the interdiffusion data. Emphasize finally that the combination of experimental observations, computer simulations and theoretical study, has been proven to be here an efficient tool for estimating the interconnection between acceleration data and experimental results under realistic microgravity conditions.

Acknowledgements

This work was supported by the MICINN under project AYA2010-11917-E, which partially covers our participation in the two active ESA projects HSF-US/2010-042 and HSF-US/2010-041.

References

- [1] D.T.J. Hurlle (Ed.), Handbook of Crystal Growth, North-Holland, Amsterdam, 1994.
- [2] H.J.V. Tyrrell, K.R. Harris, Diffusion in Liquids, Butterworths, London, 1984.
- [3] D. Herlach, P. Galenko, D. Holland-Moritz, Metastable Solids from Undercooled Melts, Elsevier, Amsterdam, 2007.
- [4] J.P. Garandet, New determinations of diffusion coefficients for various dopants in liquid silicon, Int. J. Thermophys. 28 (2007) 1285–1303.
- [5] B. Gao, X.J. Chen, S. Nakano, K. Kakimoto, Crystal growth of high-purity multicrystalline silicon using a unidirectional solidification furnace for solar cells, J. Cryst. Growth 312 (2010) 1572–1576.
- [6] A. Griesche, F. Garcia Moreno, M.-P. Macht, G. Frohberg, Chemical diffusion experiments in AlNiCe-melts, Materials Science Forum 508 (2006) 567–572.
- [7] A. Griesche, B. Zhang, J. Horbach, A. Meyer, Atomic diffusion and its relation to thermodynamic forces in Al–Ni melts, Defects Diffus. Forum 289–292 (2009) 705–710.
- [8] J. Friedrich, R. Backofen, G. Müller, Numerical simulation of formation of grain structure and global heat transport during solidification of technical alloys in MSL inserts, Adv. Space Res. 29 (2002) 549–662.
- [9] B. Zhang, A. Griesche, A. Meyer, Diffusion in Al–Cu melts studied by time-resolved X-ray radiography, Phys. Rev. Lett. 104 (2010) 035902, 4 pp.
- [10] V. Shevtsova, IVIDIL experiment onboard the ISS, Adv. Space Res. 46 (2010) 672–679.
- [11] V. Shevtsova, A. Mialdun, D. Melinkov, I. Ryzhkov, Y. Gaponenko, Z. Saghir, Y. Lyubimova, J.-C. Legros, The IVIDIL experiment onboard the ISS: Thermodiffusion in the presence of controlled vibrations, C. R. Mecanique 339 (2011) 310–317.
- [12] N. Saez, X. Ruiz, Jna Gavaldà, S. Cito, J. Pallarés, V. Shevtsova, Comparative ISS accelerometric analyses, in: Proceedings of the 63rd International Astronautical Congress, Naples, Italy, 2012.
- [13] N. Sáez, X. Ruiz, Jna Gavaldà, Accelerometric nonlinearities in the International Space Station, ISS, in: XVIII Congreso de Física Estadística, FISES 2012, Palma, Mallorca.
- [14] C.L. Nikias, A. Petropulu, Higher-Order Spectra Analysis. A Nonlinear Signal Processing Framework, Prentice Hall, 1993.
- [15] A. Rivola, P.R. White, Detecting system non-linearities by means of higher order statistics, in: 3rd International Conference of Acoustic and Vibratory Surveillance Methods and Diagnostic Techniques, Senlis, France, 1998.
- [16] A. Rivola, P.R. White, Use of higher order spectra in conditions monitoring: Simulation and experiments, in: Proceedings of the Design Engineering Technical Conferences, DETC99, Las Vegas, NV, USA, 1999 (paper CETC99/VIB-8332).
- [17] M.A.A.S. Choudhury, S.J. Shah, N.F. Thornhill, Detection and diagnosis of system nonlinearities using higher order statistics, in: 15th Triennial World Congress of the International Federation of Automatic Control, Barcelona, Spain, 2002.
- [18] J.W. Fackrell, Bispectral analysis of speech signals, Ph.D. Thesis, University of Edinburgh, 1996.
- [19] M. Boltezar, N. Jaksik, I. Simonovski, A. Kuhelj, Dynamical behavior of the planar non-linear mechanical system. Part I: Theoretical modeling, J. Sound Vib. 226 (1999) 923–940.
- [20] M. Boltezar, N. Jaksik, I. Simonovski, A. Kuhelj, Dynamical behavior of the planar non-linear mechanical system. Part II: Experiment, J. Sound Vib. 226 (1999) 941–953.

- [21] National Aeronautics and Space Administration, NASA, Reference Guide to the International Space Station, November 2010.
- [22] X. Ruiz, J. Pallarés, F.X. Grau, On the accuracy of the interdiffusion measurements at low and moderate Rayleigh numbers. A computational approach, *Int. J. Heat Mass Tran.* 53 (2010) 3708–3720.
- [23] X. Ruiz, J. Pallarés, On the accuracy of the diffusion coefficient measurements using different initial shear cell configurations at low and moderate Rayleigh numbers, *Int. J. Heat Mass Tran.* 55 (2012) 6966–6978.
- [24] S. Cito, X. Ruiz, N. Sáez, J. Pallarés, On the measurements of high temperature binary interdiffusion coefficients under the action of non-inertial ISS accelerations, in: *Proceedings of the 63rd International Astronautical Congress, Naples, Italy, 2012.*
- [25] O. Sánchez, X. Ruiz, O. Batiste, I. Mercader, Computed generated Earth diffusion processes in liquid binary Al–Cu alloys, in: *10th International Meeting of Thermodiffusion, Brussels, Belgium, 2012.*